Ultrahigh Photogain Short-Wave Infrared Detectors Enabled by Integrating Graphene and Hyperdoped Silicon

Jiang, H.; Wang, M.; Fu, J.; Li, Z.; Shaikh, M. S.; Li, Y.; Nie, C.; Sun, F.; Tang, L.; Yang, J.; Qin, T.; Zhou, D.; Shen, J.; Sun, J.; Feng, S.; Zhu, M.; Kentsch, U.; Zhou, S.; Shi, H.; Wei, X.;

Originally published:

July 2022

ACS Nano 16(2022)8, 12777-12785

DOI: https://doi.org/10.1021/acsnano.2c04704

Ultrahigh Photogain Short-Wave Infrared Detectors Enabled by Integrating Graphene and Hyperdoped Silicon

Hao Jiang[1,2], Mao Wang[3], Jintao Fu[1,4], Zhancheng Li[1], Mohd Saif Shaikh[3], YunJie Li[5,6], Changbin Nie[1,4], Feiying Sun[1], Linlong Tang[1], Jun Yang[1], Tianshi Qin[7], Dahua Zhou[1], Jun Shen[1], Jiuxun Sun[2,], Shuanglong Feng[1], Meng Zhu[8], Shengqiang Zhou[3], Haofei Shi[1,*] and Xingzhan Wei[1,4,*]*

[1]Chongqing Institute of Green and Intelligent Technology, Chinese Academy of Sciences, Chongqing 400714, China.

[2]School of Physics, University of Electronic Science and Technology of China, Chengdu 610054, China

[3]Helmholtz-Zentrum Dresden-Rossendorf, Institute of Ion Beam Physics and Materials Research, Bautzner Landstr. 400, 01328 Dresden, Germany

[4]University of Chinese Academy of Sciences, Beijing 100049, P.R. China

[5]Chongqing University of Posts and Telecommunications, Chongqing 400065, China

[6]Chongqing School, University of Chinese Academy of Sciences, Chongqing 400714, China

[7]Key Laboratory of Flexible Electronics and Institute of Advanced Materials, Nanjing Tech University, Nanjing 210009, China

[8]TianJin Jinhang Insitute of Technical Physics, Tianjin 300192, China

[*] Corresponding authors: sjx@uestc.edu.cn, shi@cigit.ac.cn, weixingzhan@cigit.ac.cn

ABSTRACT:

Highly sensitive short-wave infrared (SWIR) detectors, compatible with the silicon-based complementary metal oxide semiconductor (CMOS) process, are regarded as the key enabling components in the miniaturized system for weak signal detection. To date, the high photogain devices are greatly limited by large bias voltage, low-temperature refrigeration, narrow response band, and complex fabrication processes. Here, we demonstrate high photogain detectors working in the SWIR region at room temperature, which uses graphene for charge transport and Te-Hyperdoped Silicon (Te-Si) for infrared absorption. The prolonged lifetime of carriers, combined with the built-in potential generated at the interface between the graphene and the Te-Si, leads to ultrahigh photogain of 10^9 at room temperature (300 K) for 1.55 μm light. The gain can be improved to 10^{12}, accompanied with a detectivity of 2.1×10^{13} Jones at 80 K. Moreover, the proposed device exhibits a detectivity of 2.21×10^{11} Jones @ 300 K at the wavelength of 2.7 μm, which is far exceeding the working region of InGaAs detectors. This research shows that graphene can be used as an efficient platform for silicon-based SWIR detection, and provides a new strategy for the low-power, uncooled, high-gain infrared detectors compatible with the CMOS process.

KEYWORDS: Short-wave infrared detector, High-gain, Graphene, Te-Hyperdoped Si

INTRODUCTION

High photogain SWIR (typically ranging from 1.1 to 3 μm) detectors with an amplification of charge carriers, are regarded as the foremost elements to enable weak signal detection in many applications, such as optics communication, safety surveillance, object inspection, astronomical observation, and single-photon imaging [1-5]. The ideal SWIR detectors must combine a high photogain, broad response band, and low power consumption with facile fabrication. Early effort towards this goal is constructing avalanche photodiode (APD) based on epitaxial III-V semiconductors such as InGaAs and InAlAs, which requires high bias voltages, and the cooling operation is generally used to suppress dark currents. In addition, the working wavelength is typically restricted below 1.7 μm, and the manufacturing process is complicated due to the epitaxial crystal growth and bonding requirements [6,7]. Therefore, it is challenging for the APD device to meet the requirements of small size, light weight, and low power consumption (SWaP) of new generation SWIR detectors [8].

Recently, atomically thin two-dimensional materials, one-dimensional nanowires, and zero-dimensional quantum dots were reported to obtain high photogain under zero bias by the extraordinary electron-hole confinement [9-14]. In particular, the graphene/quantum dots hybrid photodetectors can exhibit ultrahigh photogain in the visible and near-infrared regions resulting from the photogating effect [15-23]. However, these quantum dots-based photodetectors are incompatible with the advantages of facile processing and stable performance exhibited by silicon devices.

Hyperdoped Silicon, obtained by ion implantation and/or laser annealing of silicon materials, has enabled photodetectors the advantages of wavelength expansion, high infrared light absorption, and low cost. More importantly, it inherently has the excellent compatibility with the CMOS process [24-26]. However, the short carrier lifetime caused by hyperdoping severely limit the responsivity (10^{-2}-10^{-1} A/W) and gain of the devices merely based on Hyperdoped Silicon [27].

Herein, we propose and demonstrate a hybrid architecture by integrating graphene with Te-Hyperdoped Silicon (Te-Si). The obtained photodetectors exhibit ultrahigh photogain in the SWIR region at room temperature. We clarify the physical principles that govern the operation of the graphene/Te-Si hybrid device using simulations and analytical models. The experimental and modeling results exhibit a good agreement,

which proves that the delicate integration of graphene (with high mobility and low carrier concentration) and Te-Si (with high carrier concentration) is the key to obtain the high performance. Two figure-of-merits, namely the lifetime-gain and potential-gain are proposed and verified to dominate the overall photoconductivity gain. The ultrahigh photoconductivity gain (10^{12}@80 K, 10^{9}@300 K) and detectivity (2.1×10^{13} Jones@80 K, 2.35×10^{12} Jones@300 K) at the wavelength of 1.55 μm have been obtained, which are comparable to the state-of-the-art InGaAs photodetectors. Meanwhile, the hybrid device can exhibit a detectivity of 2.21×10^{11} Jones (@300 K) at the wavelength of 2.7 μm, which is beyond the working wavelength of InGaAs devices. This hybrid device integrated with graphene and hyperdoped silicon provides a promising approach to CMOS-compatible, broadband infrared imaging at room temperature.

RESULTS AND DISCUSSION

The structural diagram of the designed graphene/Te-Si hybrid photodetector is shown in Fig. 1a. The Si layer hyperdoped by Te element is etched into stripes to avoid direct electrical contact with the gold electrodes. The patterned graphene film is connected to the electrodes and conformally covers the Te-Si stripes (See Supplementary Figure 1 about the fabrication process and device photograph). For sufficiently high impurity concentrations of Te element, a delocalized intermediate band can be formed within the bandgap of Si, as shown in Fig. 1b. This intermediate band facilitates the sub-band absorption, and the carrier excitation is viable from the intermediate band to the conduction band, which promotes the expansion of photoresponse covering the whole SWIR region. The measured absorption spectra of Te-Si with different doping concentrations are shown in Supplementary Figure 2, which shows that the wavelength is extended to 3.1 μm and the absorption is up to around 55%. The Raman and Rutherford backscattering-channeling spectrometry measurement results of Te-Si samples can be seen in Supplementary Figures 3 and 4.

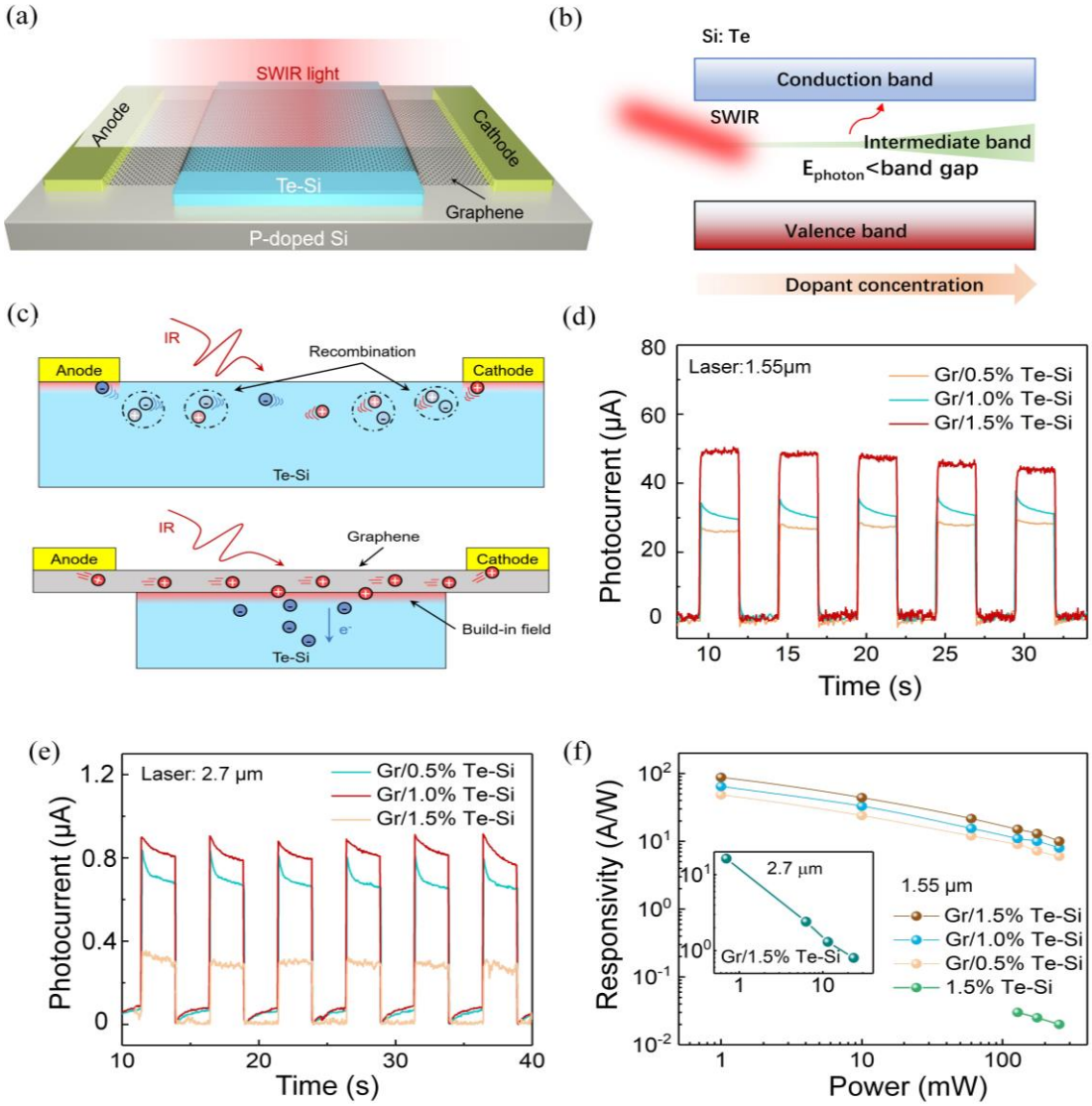

Fig. 1 Device schematic, operation principle and performance. (a) Schematic diagram of the graphene/Te-Si hybrid photodetectors. (b) Principle of sub-band gap carrier excitation in intermediate band Si. (c) Schematic views of the working mechanism of Te-Si and graphene/Te-Si hybrid device. (d) and (e) Time-dependent photoresponse of the hybrid photodetector with different doping levels of Te at the wavelength of 1.55 μm and 2.7 μm, respectively. (f) Relationship between responsivity and optical power for 1.55 μm and 2.7 μm (inset) infrared light.

Due to the existence of charged impurities in Te-Si introduced by hyperdoping, the indirect recombination becomes strong, and the lifetime of carrier is short. Therefore, when the Te-Si photoconductor is irradiated by SWIR light, only a small amount of photogenerated electron-hole pairs (mainly near the electrodes) can be utilized, as shown in the top diagram of Fig. 1c. The simple semiconductor metal junction cannot provide a high optical gain. In contrast, when the graphene is integrated with Te-Si, a large built-in potential can be formed at the interface of Te-Si and graphene,

which leads to the efficient separation of electron-hole pairs. Holes will be injected into the graphene channel to participate in a rapid recirculation, and electrons will be trapped in Te-Si, as shown in the bottom illustration of Fig. 1c. The recombination time is greatly prolonged. Aa a result, the graphene/Te-Si hybrid device obtains a photoresponse with ultrahigh gain (See Supplementary Figure 5 about more photoresponse results of the hybrid photodetector and the reference device).

The photoelectric response of graphene/Te-Si photodetector for 1.55 μm light is shown in Fig. 1d. With the increase of Te-doping, the experimentally measured photoresponse signal increases, and the largest photocurrent is obtained for the graphene/1.5% Te-Si device (See the detailed data in Supplementary Figure 6). The scanning mapping image shows that the photoresponse is primarily contributed from the integration part of graphene and Te-Si (Supplementary Figure 7). To prove the broad-band response characteristic, the photoelectric signals were measured when the radiation wavelength was extended to 2.7 μm, which exhibits an excellent repeatability under different light powers (Supplementary Figure 8). Figure. 1e shows the relevant photocurrents as a relationship of Te-doping concentration, which is consistent with the trend obtained at 1.55 μm.

The photoresponsivity can be calculated by Formula (S-1) in Supplementary information, in which the spot parameters of laser are shown in Supplementary Table 1. The relationship between the responsivity and optical power is shown in Fig. 1f. The responsivity of the graphene/1.5% Te-Si photodetector is up to 100 A/W for 1.55 μm light, at least 2 orders of magnitude higher than the reference device without graphene, which reflects the existence of large photogain phenomenon in such hybrid device. Similarly, the hybrid device can obtain a high responsivity of 16.3 A/W under at 2.7 μm, as shown in the inset of Fig. 1f.

Next, the photogain mechanism of the hybrid device is further clarified. According to the formula of lifetime-gain $\eta(\tau_r, \mu) = \frac{\tau_r}{\tau_t} = \frac{\tau_r}{L^2} \cdot \mu \cdot V$, where τ_r is the recombination lifetime, τ_t is the transit time of carriers in the channel which is as a function of channel length L, mobility μ, and external bias voltage V [28]. Thus, the measured responsivity (or photogain) of the reference device is low due to the short carrier lifetime (~picosecond) and low mobility (~56 $cm^2V^{-1}s^{-1}$) of the Te-Si material [27]. However, the lifetime-gain can be greatly improved in the hybrid device, by constructing the heterojunction between graphene and Te-Si. The heterojunction

provides a barrier to hinder the recombination of photogenerated carriers, and thereby effectively prolong the carrier lifetime. Meanwhile, the graphene sample has significantly high mobility of 11218 $cm^2V^{-1}s^{-1}$ and acts as the transmission channel, where the photogenerated carriers would transport very fast and conduct multiple cycles before recombination.

The lifetime-gain mechanism can be verified by characterizing the performance of the hybrid device under the liquid nitrogen temperature. Figure. 2a shows the photoelectric response at different temperatures with 1.55 μm laser illumination. It can be seen that the photocurrent increases as the decrease of temperature. Moreover, with the increase of photocurrent, the falling edge of the response time curve is obviously extended, which means the recombination lifetime τ_r is prolonged to 2.6 s. The inset in Fig. 2a highlights the variation of photocurrent versus time, which hints that photocurrent is closely correlated with the recombination life of photogenerated carriers.

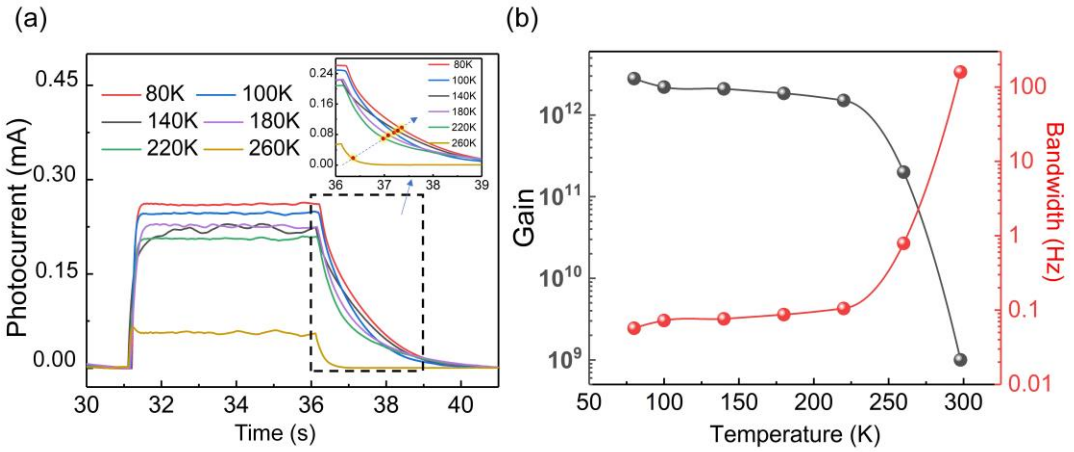

Fig. 2 Characteristics of the hybrid device at low temperature. (a) Photoresponse of the hybrid photodetector at different temperatures for 1.55 μm light irradiation. The optical power is 60 mW. (b) Photogain (black) and bandwidth (red) as a relationship of temperature.

According to the gain formula $G = \frac{QE \cdot \mu \cdot V \cdot \tau_r}{A}$ [29], where QE represents the quantum efficiency, V and A denote the bias voltage and device area, respectively. It can be calculated that the gain is 10^{12} at 80 K and 10^9 at room temperature (300 K), respectively, as shown in Fig. 2b. The relationship between bandwidth and temperature is also provided, which proves that the bandwidth is inversely proportional to the gain. Thus, it is worthy to note that the increase of gain is at the cost of response speed. However, the response speed of the hybrid photodetector is still 4 orders of magnitude higher than the Te-Si photodetector (see Supplementary Figure 7). The slow response of Te-Si

photodetector is because the photogenerated carriers continuously generated under infrared light can only reach the electrodes by diffusion motion. The fast response speed of hybrid device can be attributed to the usage of high mobility graphene as a channel in substitution for Te-Si, which can greatly shorten the transit time τ_t of carriers.

In addition to the lifetime-gain, the potential-gain is also another important factor that influences the photogain. When Te-Si is integrated with graphene, a contact potential ψ_s will be formed at the interface due to the doping discrepancies [30]. To derive the contact potential, the relationship between the energy band of the silicon/graphene interface and the position (z) is obtained by solving the Poisson equation (S-2) in Supplementary information. Figs. 3a and 3b shows the band diagram of silicon-graphene junction for $N = 1\times10^{20}$ cm^{-3} and $N = 1\times10^{17}$ cm^{-3}, respectively. According to equations (S-3)-(S-5) in Supplementary information, the relationship between the contact potential and the carrier concentration of silicon and graphene can be expressed as

$$\psi_s - \frac{q^2}{2\epsilon_s N}\left[\frac{(\Delta-\psi_s)^2}{\pi(\hbar v_F)^2} - n_0\right]^2 = 0 \qquad (1)$$

where n_0 is the carrier concentration of graphene, Δ is the difference of work functions of the two materials, ϵ_s is the dielectric constant of silicon, q is the single-electron charge, v_F is the Fermi velocity, and $\hbar$ is the Planck constant. According to the derivation above, it is found that the contact potential and depletion width of the interface can be altered by changing the silicon carrier concentration N (as shown in Fig. 3b. Furthermore, the variation of depletion region width (w) and contact potential (ψ_s) with carrier concentration can be calculated, as shown in Figs. 3c and 3d, respectively. It can be seen that with the increase of carrier concentration in silicon, the depletion region width becomes smaller, and the contact potential would gradually increase. Moreover, the low carrier concentration (n) in graphene is beneficial to obtain large contact potential. For the case without bias voltage, the contact potential is equivalent to the built-in potential. The enhancement of the built-in potential will be more conducive to the separation of photogenerated carriers.

In order to investigate the relationship between carrier concentration and built-in potential more intuitively, the interface contact model between silicon and graphene is established, and the distribution of built-in potential is simulated when the silicon carrier concentration is 1×10^{20} cm^{-3} (Fig. 3e), 1×10^{18} cm^{-3} (Fig. 3f), and 1×10^{16} cm^{-3}

(Fig. 3g), respectively. It can be seen that with the increase of silicon carrier concentration, the depletion region becomes narrower, and the built-in potential increases significantly. It can be found from the simulation results that the built-in potential can be improved by reducing the carrier concentration of channel material (graphene) and increasing the carrier concentration of light-absorbing material (Te-Si).

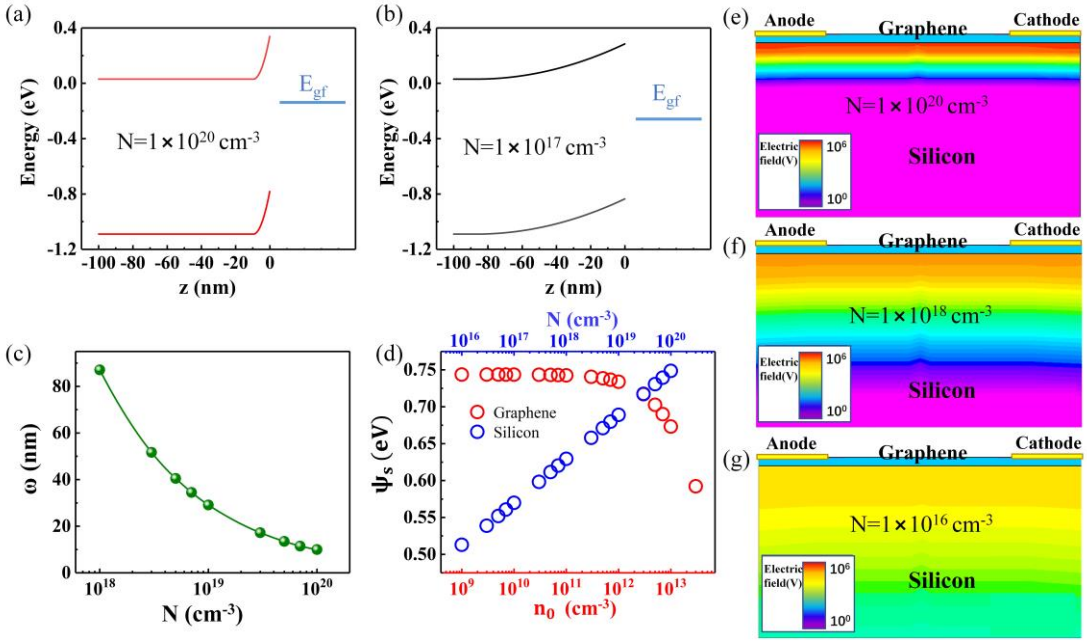

Fig. 3 Relationship between contact potential and carrier concentration. (a) and (b) Band diagrams of silicon-graphene junction for $N = 1\times10^{20}$ cm^{-3} and $N = 1\times10^{17}$ cm^{-3}, respectively. (c) Relationship between the width of depletion zone and silicon doping concentration. (d) Simulated contact barrier (ψ_s) as a function of graphene carrier concentration (n_0) and silicon carrier concentration (N). (e)-(f) Simulated built-in electric field distributions in heterojunction with different doping concentration of silicon.

In order to verify the influence of potential factor on gain, the performance of graphene/Te-Si junction by gate modulation was characterized. The schematic view of testing configuration is shown in Fig. 4a. Figure. 4b depicts the energy band diagram of graphene/Te-Si interface without bias voltage, which indicates that the built-in potential ($e\Phi_i$) is generated by the contact potential ($e\psi_s$). In contrast, when a reverse bias voltage is applied, more electrons will be injected into graphene and the built-in potential will be increased to $e(\Phi_i + V)$, as shown in Fig. 4c.

The time-dependent photoresponse with different reverse gate biases was measured, and the response curves related with 1.55 μm and 2.7 μm light illumination are shown in Figs. 4d and 4e, respectively. The photocurrent increases significantly with the increase of gate voltage. The relationship between responsivity and gate voltage is

shown in Fig. 4f. The photoresponsivity is enhanced by nearly 7 times by increasing the reverse bias voltage, which is because that the reverse bias voltage can effectively improve the built-in potential of the heterojunction. Differently, the positive bias voltage has a tiny influence on the built-in potential, and consequently, the responsivity nearly does not change. It can be found that the improvement of built-in potential can enhance the optoelectronic performance of the hybrid device, and the relevant potential-gain can be defined as $\omega(\psi_s(N, n_0))$.

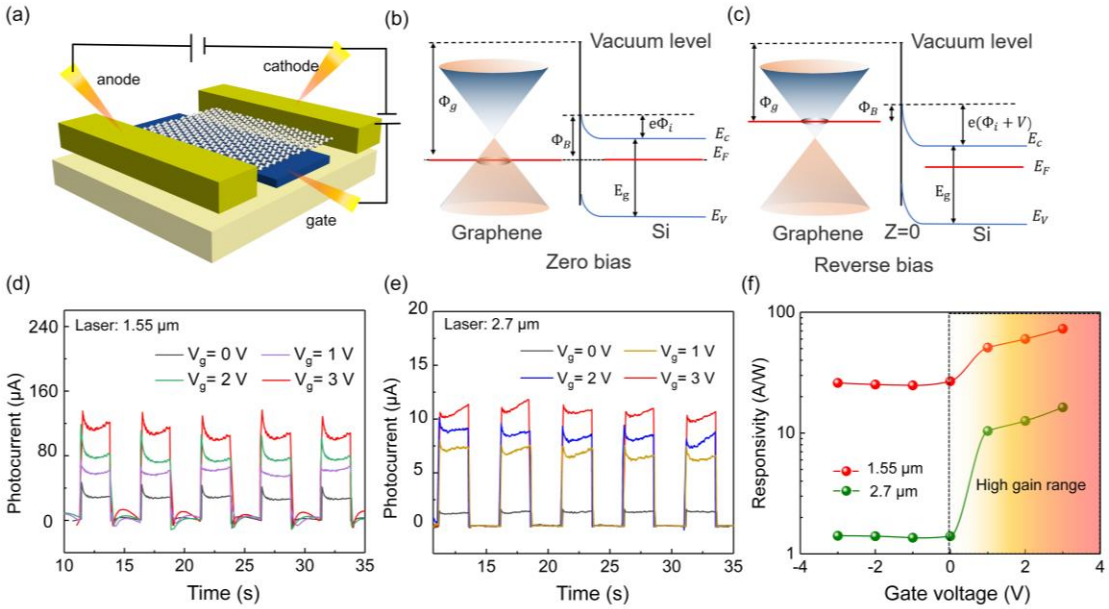

Fig. 4 Effect of built-in potential on photogain. (a) Device configuration of the gate-modulated graphene/Te-Si junction. The source and drain electrodes are connected to the ends of the graphene channel, and the gate contacts the Te-Si. (b) and (c) Energy band diagrams of graphene/Te-Si junction when without or with reverse bias voltage, respectively. (d) and (e) Time-dependent photoresponse for the 1.55 μm and 2.7 μm light with different reverse gate bias. (f) Relationship between photoresponsivity and gate voltage.

Overall, this ultrahigh photogain in the hybrid device can be explained by redefining the optical gain, which is expressed $G = \eta(\tau_r, \mu) \cdot \omega(\varphi_i(N, n_0))$. Two figure-of-merits, namely the lifetime-gain factor $\eta(\tau_r, \mu)$ and the potential-gain factor $\omega(\varphi_i(N, n_0))$, are specifically proposed to dominate the photoconductivity gain G. We have demonstrated that the lifetime-gain factor is mainly determined by the recombination lifetime τ_r and the mobility of conduction carriers μ, and the potential-gain factor is mainly influenced by the carrier concentrations N and n_0 of Te-Si and graphene

To characterize the noise-related performance, the noise power spectral density of

the hybrid photodetector and Te-Si device was measured, as shown in Fig. 5a. The noise power spectral density $S(f)$ of the hybrid devices is obviously smaller. Furthermore, the noise voltage V_n was obtained by the formula $V_n = \sqrt{\int_{f1}^{f2} S(f)\, df}$, where $S(f)$ is the noise power spectral density, $f1$ and $f2$ are the interval boundaries of the integral frequency band, as shown in Fig. 5b. We can find that the hybrid photodetector is around 10 times smaller than the Te-Si device at different bias voltage. More detailed comparison data can be seen in Supplementary Figures 9， 10 and Table 2. This phenomenon can be attributed to the defects is inevitably introduced in Te-Si material in the ion implantation process, which brings in more 1/f noise through capturing or emitting carriers [31].

Further, the detectivity can be obtained by the formula $D^* = \frac{\mathrm{R_p}}{V_n} \times \mathrm{R_{es}}$, where R_p is the responsivity, R_{es} is the device resistance. The D^* of hybrid photodetector can reach 2.35×10^{12} Jones (@100 Hz, 1.55 μm) at room temperature, and can be improved to 2.1×10^{13} Jones at low temperature (80 K). These values are not only 10^5 times higher than that of Te-Si photodetector (3.3×10^7 Jones in Supplementary Table 3), but also comparable to the classical InGaAs photodetectors (7.4×10^{11} Jones@ 295K, and 1.5×10^{13} Jones@ 253 K) [32]. More significantly, the response wavelength of the hybrid device here can be extended to 2.7 μm, which is superior to InGaAs detectors restricted below 1.7 μm, and D^* can reach 2.21×10^{11} Jones (@100 Hz) at room temperature. Other photodetectors integrated with graphene and other materials are also compared, which can prove that the graphene/Te-Si device herein can exhibit competitive performance in detectivity, responsivity, and response wave band, as shown in Figs. 5c and 5d [33-38]. More detailed comparison data can be seen in Supplementary Table 4. The outstanding performance of ultrahigh photogain, broad response band, and low power consumption with facile fabrication, renders the graphene/Te-Si hybrid device a promising application prospect in a series of fields, such as biological imaging, medical sensing, and low light level photography [39,40].

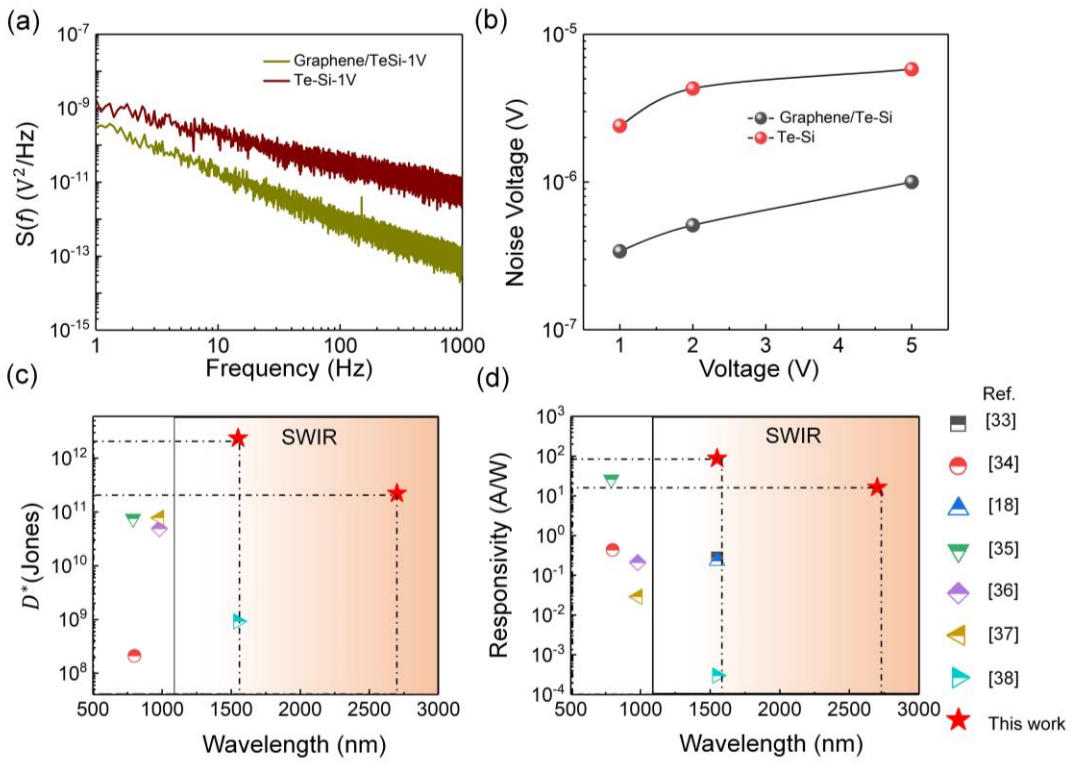

Fig. 5 Performance comparison. (a) Comparison of the noise power spectral density between graphene/Te-Si hybrid photodetector and Te-Si device at the bias voltage of 1V. (b) Noise voltages under different bias voltages for the hybrid and Te-Si photodetectors. (c) Detectivity and (d) responsivity obtained in this work which are compared with those of related devices reported in the literatures.

CONCLUSION

In this paper, a graphene/Te-Si heterostructure has been proposed and demonstrated to obtain ultrahigh gain in the SWIR band. The excellent performance has been proved to relate with the prolongated carrier lifetime and the built-in potential in the heterojunction. The hybrid photodetector with a high responsivity of 100 A/W and ultrahigh D* of 2.35×10^{12} Jones at 1.55 μm has been experimentally proved at room temperature. Moreover, the fabrication of such heterostructure device is fully compatible with the silicon-based CMOS process, which paves the way for the realization of miniaturized high-gain infrared detectors.

METHODS

Device Fabrication

For the fabrication of photodetectors, the lightly p-doped silicon wafer with a thickness of 380 μm was selected as the substrate. A 150 nm thick Te-Si layer with

epitaxial recrystallization was obtained on the silicon substrate by ion implantation combined with a pulsed laser melting process [24]. The photoresist AZ3100 was spin-coated onto the Te-Si layer, and subsequently exposed by photolithography, and developed in AZ300 solution, leading to the forming of stripe patterns. After that, the Te-Si layer unprotected by photoresist was etched by sulfur hexafluoride gas, so that the bottom p-doped silicon was exposed. Lastly, the isolated Te-Si stripe patterns were obtained by degumming.

The graphene film was synthesized by the chemical vapor deposition method on Cu foil. Subsequently, the graphene was spin-coated with polymethylmethacrylate (PMMA) and baked on a hot plate at 150 ℃ for 10 minutes. A mixed solution of hydrochloric acid and hydrogen peroxide was used as an etchant to remove the copper film. Then, the graphene was fished out with the treated substrate and dried, and finally, the PMMA film was dissolved with acetone.

To fabricate the electrodes, two photoresists, LOR and S1805, were successively spin-coated on the surface of graphene. After that, the samples were exposed and developed. Cr film (3 nm) and Au film (50 nm) were sputtered on the surface of graphene by magnetron sputtering. Electrodes distributed on the lightly p-doped silicon layer were obtained by dissolving the unexposed photoresist with acetone solution.

A bi-layer (LOR and S1805) photolithography process was used to pattern the graphene film. After development, the uncovered graphene was removed by using oxygen etching for about 30 s. Lastly, the graphene channels were obtained by dissolving the remaining photoresist in AZ400 solution, which conformally cover the Te-Si stripes and connect with the electrodes

Characterization Methods

The mobility and carrier concentration of graphene was measured by HMS-TT-MAN Hall effect test system. The noise data were obtained from the noise power spectral density collected by the noise tester (Shenzhen Liangwei Co., Ltd). The photoelectric properties at room temperature were measured by Keithley semiconductor tester (SCS4200) combined with 1.55 and 2.7 μm lasers. The photoelectric performance at low temperature was acquired by SCS1500 in a liquid nitrogen refrigeration platform equipped with a 1.55 μm laser. The response time was measured by SCS7510, which can ensure the accurate measurement of optical response

in a small amplitude.

DECLARATION OF COMPETING INTEREST

The authors declare that they have no known competing financial interests or personal relationships that could have appeared to influence the work reported in this paper.

ACKNOWLEDGEMENTS

This work was supported by the National Key R&D Program of China (2017YFE0131900), Natural Science Foundation of Chongqing, China (cstc2019jcyjjqX0017), and Chongqing Talents Innovation and Entrepreneur Leaders Project (CQYC201903020). M. Wang and M. S. Shaikh acknowledge the financial support by Deutsche Forschungsgemeinschaft (WA4804/1-1).

AUTHOR CONTRIBUTIONS

H.J. and X.W. conceived the idea. H. J. carried out simulations and experiments including device fabrication and performance characterization with the help from J.F., Y.L., C.N., F.S., L.T., J.Y., T.Q., D.Z., J.S., S.F., and M.Z. M.W., M.S., and S.Z. contributed Te-Si materials and characterization results. Z.L. synthesized and characterized the graphene samples. H.J. and X.W. wrote the manuscript with comments from all the other authors including H.S., M.W., S.Z., J.F., etc. J.S., H.S., and X.W. supervised the project.

ADDITIONAL INFORMATION

Supplementary Information accompanies this paper at https:xxxxx

REFERENCES

[1] Thimsen, E., Sadtler, B. & Berezin, M. Y. Shortwave-infrared (SWIR) emitters for biological imaging: a review of challenges and opportunities. Nanophotonics 6, 1043-1054 (2017).

[2] Hong, G. S., Antaris, A. L. & Dai, H. J. Near-infrared fluorophores for biomedical imaging. Nature Biomedical Engineering 1 (2017).

[3] Kenry, Duan, Y. & Liu, B. Recent Advances of Optical Imaging in the Second Near-Infrared Window. Advanced materials 30 (2018).

[4] Liu, F., Liang, Y. J., Chen, Y. F. & Pan, Z. W. Divalent Nickel-Activated Gallate-Based Persistent Phosphors in the Short-Wave Infrared. Advanced Optical Materials 4, 562-566 (2016).

[5] Pradhan, S., Dalmases, M. & Konstantatos, G. Solid-State Thin-Film Broadband Short-Wave Infrared Light Emitters. Advanced materials 32 (2020).

[6] Nada, M. et al. Inverted InAlAs/InGaAs Avalanche Photodiode with Low-High-Low Electric Field Profile. Japanese Journal of Applied Physics 51 (2012).

[7] Ma, Y. J. et al. Impact of etching on the surface leakage generation in mesa-type InGaAs/InAlAs avalanche photodetectors. Optics Express 24, 7823-7834 (2016).

[8] Rogalski, A., Martyniuk, P. & Kopytko, M. Challenges of small-pixel infrared detectors: a review. Reports on Progress in Physics 79 (2016).

[9] Novoselov, K. S. et al. Two-dimensional atomic crystals. Proceedings of the National Academy of Sciences of the United States of America 102, 10451-10453 (2005).

[10] Hu, J. T., Odom, T. W. & Lieber, C. M. Chemistry and physics in one dimension: Synthesis and properties of nanowires and nanotubes. Accounts of Chemical Research 32, 435-445 (1999).

[11] Tans, S. J., Verschueren, A. R. M. & Dekker, C. Room-temperature transistor based on a single carbon nanotube. Nature 393, 49-52 (1998).

[12] Zheng, D. S. et al. When Nanowires Meet Ultrahigh Ferroelectric Field-High-Performance Full-Depleted Nanowire Photodetectors. Nano letters 16, 2548-2555 (2016).

[13] Chen, Y. F. et al. Unipolar barrier photodetectors based on van der Waals heterostructures. Nature Electronics 4, 357-363 (2021).

[14] Tong, L. et al. Stable mid-infrared polarization imaging based on quasi-2D tellurium at room temperature. Nature communications 11 (2020).

[15] Ackerman, M. M., Tang, X. & Guyot-Sionnest, P. Fast and Sensitive Colloidal Quantum Dot Mid-Wave Infrared Photodetectors. ACS nano 12, 7264-7271 (2018).

[16] Ni, Z. et al. Plasmonic Silicon Quantum Dots Enabled High-Sensitivity Ultrabroadband Photodetection of Graphene-Based Hybrid Phototransistors. ACS nano 11, 9854-9862 (2017).

[17] Tsai, T. H. et al. Photogating WS2 Photodetectors Using Embedded WSe2 Charge Puddles. ACS nano 14, 4559-4566 (2020).

[18] Chen, Z. et al. High Responsivity, Broadband, and Fast Graphene/Silicon Photodetector in Photoconductor Mode. Advanced Optical Materials 3, 1207-1214 (2015).

[19] Jiang, H. et al. Ultrasensitive and fast photoresponse in graphene/silicon-on-insulator hybrid structure by manipulating the photogating effect. Nanophotonics 9, 3663-3672 (2020).

[20] Goykhman, I. et al. On-Chip Integrated, Silicon-Graphene Plasmonic Schottky Photodetector with High Responsivity and Avalanche Photogain. Nano letters 16, 3005-3013 (2016).

[21] Liu, F. Z. & Kar, S. Quantum Carrier Reinvestment-Induced Ultrahigh and Broadband Photocurrent Responses in Graphene - Silicon junctions. ACS nano 8, 10270-10279 (2014).

[22] Bera, K. P. et al. Graphene Sandwich Stable Perovskite Quantum-Dot Light-Emissive Ultrasensitive and Ultrafast Broadband Vertical Phototransistors. ACS nano 13, 12540-12552 (2019).
[23] Tang, X., Ackerman, M. M., Chen, M. & Guyot-Sionnest, P. Dual-band infrared imaging using stacked colloidal quantum dot photodiodes. Nature Photonics 13, 277-282 (2019).
[24] Branz, H. M. et al. Nanostructured black silicon and the optical reflectance of graded-density surfaces. Applied Physics Letters 94 (2009).
[25] Oh, J., Yuan, H. C. & Branz, H. M. An 18.2%-efficient black-silicon solar cell achieved through control of carrier recombination in nanostructures. Nature nanotechnology 7, 743-748 (2012).
[26] Carey, J. E., Crouch, C. H., Shen, M. Y. & Mazur, E. Visible and near-infrared responsivity of femtosecond-laser microstructured silicon photodiodes. Optics Letters 30, 1773-1775 (2005).
[27] Wang, M. et al. Extended Infrared Photoresponse in Te-Hyperdoped Si at Room Temperature. Physical Review Applied 10 (2018).
[28] Fang, H. & Hu, W. Photogating in Low Dimensional Photodetectors. Advanced science 4, 1700323 (2017).
[29] Konstantatos, G. et al. Hybrid graphene-quantum dot phototransistors with ultrahigh gain. Nature nanotechnology 7, 363-368 (2012).
[30] Li, T. et al. Spatially controlled electrostatic doping in graphene p-i-n junction for hybrid silicon photodiode. npj 2D Materials and Applications 2 (2018).
[31] Fang, Y. J., Armin, A., Meredith, P. & Huang, J. S. Accurate characterization of next-generation thin-film photodetectors. Nature Photonics 13, 1-4 (2019).
[32] Huo, N. J. & Konstantatos, G. Recent Progress and Future Prospects of 2D-Based Photodetectors. Advanced materials 30, (2018).
[33] Amirmazlaghani, M., Raissi, F., Habibpour, O., Vukusic, J. & Stake, J. Graphene-Si Schottky IR Detector. Ieee Journal of Quantum Electronics 49, 589-594 (2013).
[34] An, X. H., Liu, F. Z., Jung, Y. J. & Kar, S. Tunable Graphene-Silicon Heterojunctions for Ultrasensitive Photodetection. Nano letters 13, 909-916 (2013).
[35] Huang, K. et al. High and Fast Response of a Graphene-Silicon Photodetector Coupled with 2D Fractal Platinum Nanoparticles. Advanced Optical Materials 6 (2018).
[36] Zhang, T. F. et al. Broadband photodetector based on carbon nanotube thin film/single layer graphene Schottky junction. Scientific reports 6 (2016).
[37] Selvi, H., Hill, E. W., Parkinson, P. & Echtermeyer, T. J. Graphene-silicon-on-insulator (GSOI) Schottky diode photodetectors. Nanoscale 10, 18926-18935 (2018).
[38] Wang, M. et al. Silicon-Based Intermediate-Band Infrared Photodetector Realized by Te Hyperdoping. Advanced Optical Materials 9 (2021).
[39] Yotter, R. A. & Wilson, D. M. A review of photodetectors for sensing light-emitting reporters in biological systems. Ieee Sensors Journal 3, 288-303 (2003).
[40] Lochner, C. M., Khan, Y., Pierre, A. & Arias, A. C. All-organic optoelectronic sensor for pulse oximetry. Nature communications 5 (2014).